The Astrophysical Journal, 892:2 (7pp), 2020 March 20 https://doi.org/10.3847/1538-4357/ab7819

Effects of Orbital Eccentricity and IMF Cone Angle on the Dimensions of Mercury's Magnetosphere

J. Zhong[1], J.-H. Shue[2], Y. Wei[1], J. A. Slavin[3], H. Zhang[1], Z. J. Rong[1], L. H. Chai[1], and W. X. Wan[1]
[1] Key Laboratory of Earth and Planetary Physics, Institute of Geology and Geophysics, Chinese Academy of Sciences, Beijing, People's Republic of China
j.zhong@mail.iggcas.ac.cn
[2] Institute of Space Science, National Central University, Taoyuan, Taiwan
[3] Department of Climate and Space Sciences and Engineering, University of Michigan, Ann Arbor, MI, USA
Received 2019 October 25; revised 2020 February 15; accepted 2020 February 18; published 2020 March 19

Abstract

We investigate the influence of orbital eccentricity and interplanetary magnetic field (IMF) direction on the dimensions of Mercury's magnetosphere using four Earth years of data collected by the *MErcury Surface, Space ENvironment, GEochemistry, and Ranging* spacecraft. The variations in magnetopause subsolar distance, flank distance, and tail radius are compared to determine the global dimensions and compressibility of the magnetosphere. As Mercury moves from perihelion (aphelion) to aphelion (perihelion) its magnetosphere expands (contracts) globally by ∼15% on average. After mapping all of the magnetopause crossings to a fixed radial distance from the Sun, we find that IMF cone angle changes lead to reconfigurations of the magnetosphere of comparable magnitude to radial solar distance effects. Furthermore, the magnetosphere is found to expand globally under the quasi-radial IMF, while contracting under the quasi-perpendicular conditions. A new Mercury magnetopause model parameterized by the heliocentric distance and IMF cone angle was constructed. Unlike Earth, the model gives a closed magnetopause for the nightside in most cases, and its flaring decreases with the contraction of the magnetosphere. The results demonstrate the highly variable reconfigurations of Mercury's magnetosphere under its extreme environmental conditions.

Unified Astronomy Thesaurus concepts: Planetary magnetosphere (997); Solar-planetary interactions (1472); Mercury (planet) (1024); Solar wind (1534); Interplanetary magnetic fields (824); Solar magnetic reconnection (1504)

1. Introduction

Mercury has a relatively weak global magnetic field that is about 1% the strength of Earth's and the dipole field is offset by ∼0.2 R_M (where R_M is Mercury's mean radius, 2440 km) to the north (Anderson et al. 2011). Under normal conditions, the planetary magnetic field can deflect the solar wind around the planet, creating a miniature terrestrial-type magnetosphere. The size of the magnetosphere is, on average, only about 5% of the Earth's, and a large fraction of its volume is occupied by the planet itself (e.g., Winslow et al. 2013; Zhong et al. 2015a). Unlike Earth, Mercury lacks an ionosphere, and its magnetosphere is tightly coupled to its surface-bounded exosphere, creating a unique planetary space environment (e.g., Milillo et al. 2005; Orsini et al. 2007). Global simulations have shown that the interplanetary magnetic field (IMF) orientation and solar wind dynamic pressure have a dramatic effect on Mercury's magnetospheric configuration and thus the magnetosphere–exosphere-surface coupling (e.g., Kabin et al. 2000; Ip & Kopp 2002; Kallio & Janhunen 2003; Massetti et al. 2007; Varela et al. 2015).

In situ orbital observations from *MErcury Surface, Space ENvironment, GEochemistry, and Ranging* (*MESSENGER*) have provided a wealth of data to investigate the geometry and the large-scale dynamics of Mercury's magnetosphere. The outer boundary of the magnetosphere is the magnetopause. Based on the mean magnetopause locations during the first 3 Earth years of the *MESSENGER* orbital data, Zhong et al. (2015a) developed a three-dimensional asymmetric model of Mercury's average magnetopause. This data-driven model exhibits deep near-cusp indentations of the dayside magnetopause and elongation of the magnetotail cross section in the north–south direction. This model also predicts that the offset planetary magnetic field middle latitudes in the southern hemisphere are not sufficient to deflect the solar wind from the surface. During extreme solar wind conditions, such as interplanetary coronal mass ejections (ICMEs) or high-speed streams, the entire dayside magnetosphere can be highly compressed close to the surface of Mercury (e.g., Slavin et al. 2014, 2019; Winslow et al. 2017; Jia et al. 2019). In rare cases, the dayside magnetosphere is so extremely compressed and/or eroded by reconnection-driven magnetic flux transfer to the tail that the magnetopause, if it still exists, lies below the *MESSENGER* spacecraft orbital trajectory (Zhong et al. 2015a; Slavin et al. 2019). During such "disappearing dayside magnetosphere" events, the Earth-like global magnetosphere collapsed, creating a new type of solar wind–planet interaction that is still largely unknown.

The physics of large-scale reconfigurations of the magnetosphere have been extensively investigated for Earth. To first order, the location of the magnetopause is known to be determined from the balance between the outer solar wind dynamic pressure and the inner planetary magnetic field pressure. In addition, the orientation of the IMF also contributes the pressure imbalance. When the IMF turns southward, the dayside magnetopause can move Earthward due to reconnection-driven erosion (Aubry et al. 1970; Holzer & Slavin 1978) alone or in combination with the enhancement of total pressure just outside the magnetopause (Shue & Chao 2013). The opposite effect, namely, the expansion

of the magnetopause for unusual flow-aligned IMF conditions, has also been reported. The dayside expansion can be either locally in a bullet-like shape due to the decreased total pressure in the subsolar magnetosheath (e.g., Fairfield et al. 1990; Merka et al. 2003; Samsonov et al. 2017), or globally, as a result of decreases in the total pressure in the entire magnetosheath during quasi-radial IMF conditions (e.g., Dušík et al. 2010; Suvorova et al. 2010; Park et al. 2016; Zhang et al. 2019).

The upstream solar wind at Mercury differs substantially from the average conditions at 1 au in two aspects. One is the significant long-term variations of solar wind forcing as Mercury follows its highly eccentric orbit with distances to the Sun between 0.31 and 0.47 au. The solar wind dynamic pressure varies inversely as the square of the distance from the Sun (e.g., Burlaga 2001). As Mercury moves from aphelion to perihelion, the mean solar wind dynamic pressure can more than double, which leads to a modulation of the dimensions and internal conditions within Mercury's magnetosphere on the timescale of a Mercury year (i.e., 88 Earth days). The second aspect is the IMF's greater intensity and more radial orientation than the Earth orbit. Due to the close-in nature of Mercury's orbit, the angle of Parker spiral to the direction of the solar wind flow is only ~20°, compared to ~45° at Earth (e.g., Korth et al. 2011; James et al. 2017; Chang et al. 2019). Hence, the strong radial IMF occurs much more frequently at Mercury than Earth. Previous statistical analysis of earlier *MESSENGER* near subsolar magnetopause crossings provide strong evidence that Mercury's distance from the Sun has a great effect on the subsolar distance of the dayside magnetopause (Zhong et al. 2015b; Johnson et al. 2016). In this paper the variations in subsolar distance, flank distance, and tail radius of Mercury's magnetosphere observed by *MESSENGER* are measured and used to determine the global dimensions and compressibility of the magnetosphere. After scaling the magnetopause crossings to a fixed radial distance from the Sun, it is shown that the reconfigurations of Mercury's magnetosphere driven by IMF cone angle are comparable to those resulting from changing heliocentric distance.

2. Data and Methods

The *MESSENGER* spacecraft was inserted into a highly eccentric, ~80° inclination orbit about Mercury in 2011 March, then impacted the surface in 2015 April after exhausting its fuel. *MESSENGER*'s orbit sampled all local times during the course of a Mercury year and provided excellent spatial coverage of the magnetopause surface (Bedini et al. 2012). The magnetopause crossings can be identified (DiBraccio et al. 2013; Zhong et al. 2015a) by an abrupt change in the strength and/or the direction of the magnetic field as the spacecraft crosses the current layer, or assisted by a sharp boundary in the heated ion flux spectrogram between the magnetosheath and the magnetosphere. Using the same magnetopause identification criteria as Zhong et al. (2015a), we updated the list of *MESSENGER* magnetopause crossings to cover the entire orbital duration. A total of 8086 magnetopause passes were identified by visual inspection. For magnetopause traversals with multiple crossings, due to transient oscillations of the magnetopause boundary, the mean magnetopause location of the innermost and outermost crossings was determined for the analysis.

All the data were analyzed in the aberrated Mercury solar magnetospheric (MSM) coordinate system, where the X-axis is directed from Mercury's offset magnetic dipole center toward the Sun, the Z-axis is normal to Mercury's orbital plane and points northward, and the Y-axis completes the right-handed system. We rotated the X and Y axes to account for Mercury's orbital motion with respect to an average radial solar wind velocity of 400 km s^{-1}, producing an X-axis opposite to the solar wind flow in Mercury's frame.

To quantify the size and global variability of Mercury's magnetosphere, we selected magnetopause crossings in three regions using the mean magnetopause locations: subsolar [$\cos^{-1}(X_{\rm MSM}/r) < 25°$], flank [$\cos^{-1}(|Y_{\rm MSM}|/r) < 15°$], and the tail in the southern high-latitude region [$-3\,R_{\rm M} < X_{\rm MSM} < -2\,R_{\rm M}$ and $\cos^{-1}\left(-Z_{\rm MSM}\Big/\sqrt{Y_{\rm MSM}^2+Z_{\rm MSM}^2}\right) < 30°$]. To investigate the long-term variability of Mercury's magnetosphere, the ICME intervals (Winslow et al. 2017) were excluded from this study. A total of 557, 510, and 555 magnetopause passes in three regions, respectively, were collected (Figure 1).

The dimensions of magnetosphere in the three regions are defined as subsolar point distance, flank point distance, and tail radius in the north–south direction at a distance of 2.5 $R_{\rm M}$ downstream of Mercury, as denoted by $d_{\rm subsolar}$, $d_{\rm flank}$, and $d_{\rm tail}$ in Figure 1. The solid lines give the average magnetopause from the three-dimensional magnetopause surface model (Zhong et al. 2015a):

$$r(\theta,\varphi) = r_0\left(\frac{2}{1+\cos\theta}\right)^{\alpha+\beta\cdot\cos^2\varphi} - d_0\cdot\exp\left[-\frac{1}{2}\left(\frac{\theta-\theta_0}{\Delta_\theta}\right)^2\right]\cdot\sum_{\varphi_0=\pm\pi/2}\exp\left[-\frac{1}{2}\left(\frac{\varphi-\varphi_0}{\Delta_\varphi}\right)^2\right],$$

where $r_0 = 1.51\ R_{\rm M}$, $\alpha = 0.48$, $\beta = -0.10$, $d_0 = 0.64\ R_{\rm M}$, $\theta_0 = 1.00$, $\Delta_\theta = 0.29$, and $\Delta_\varphi = 0.48$. The first term on the right side of the function is expanded from the Shue et al. (1997) functional form to describe the azimuthal asymmetry of the magnetopause, and the second term describes the near-cusp indentations by a two-dimensional Gaussian function. Our analysis uses the ratio of the observed dimensions to the average dimensions from the model, $d_{\rm obs}/d_{\rm mod}$, where $d_{\rm mod} = 1.51\ R_{\rm M}$, $1.98\ R_{\rm M}$, and $2.72\ R_{\rm M}$ for three regions, respectively. The $d_{\rm obs}/d_{\rm mod}$ is approximate to the ratio of the radial distance of the observations to the modeled average surface in the direction of the observed crossings for the subsolar and flank regions, and the ratio of the distance in Y–Z plane for the tail region. Comparison of each ratio in different regions allows us to check if the dimension or geometry of the magnetosphere is varying globally or locally.

3. Orbital Eccentricity Effect

The ratio $d_{\rm obs}/d_{\rm mod}$ is plotted as a function of Mercury heliocentric distance in Figure 2. The magnetopause crossings in three regions did not cover all the orbital heliocentric distance because of the orbit phase of *MESSENGER*. The large deviations contribute to the effect of the instantaneous variations of solar wind conditions. To emphasize the spatial trends, the data were fitted by a geometric model ($y = a_0\cdot x^{a1} + a_2$). The standard errors of the best-fit values for the three regions are 0.07 $R_{\rm M}$, 0.08 $R_{\rm M}$, and 0.10 $R_{\rm M}$, respectively. This shows that the three-dimensional magnetopause model presents the average magnetopause geometry at ~0.38 au where $d_{\rm obs}/d_{\rm mod} \approx 1$. The linear dimensions of three regions

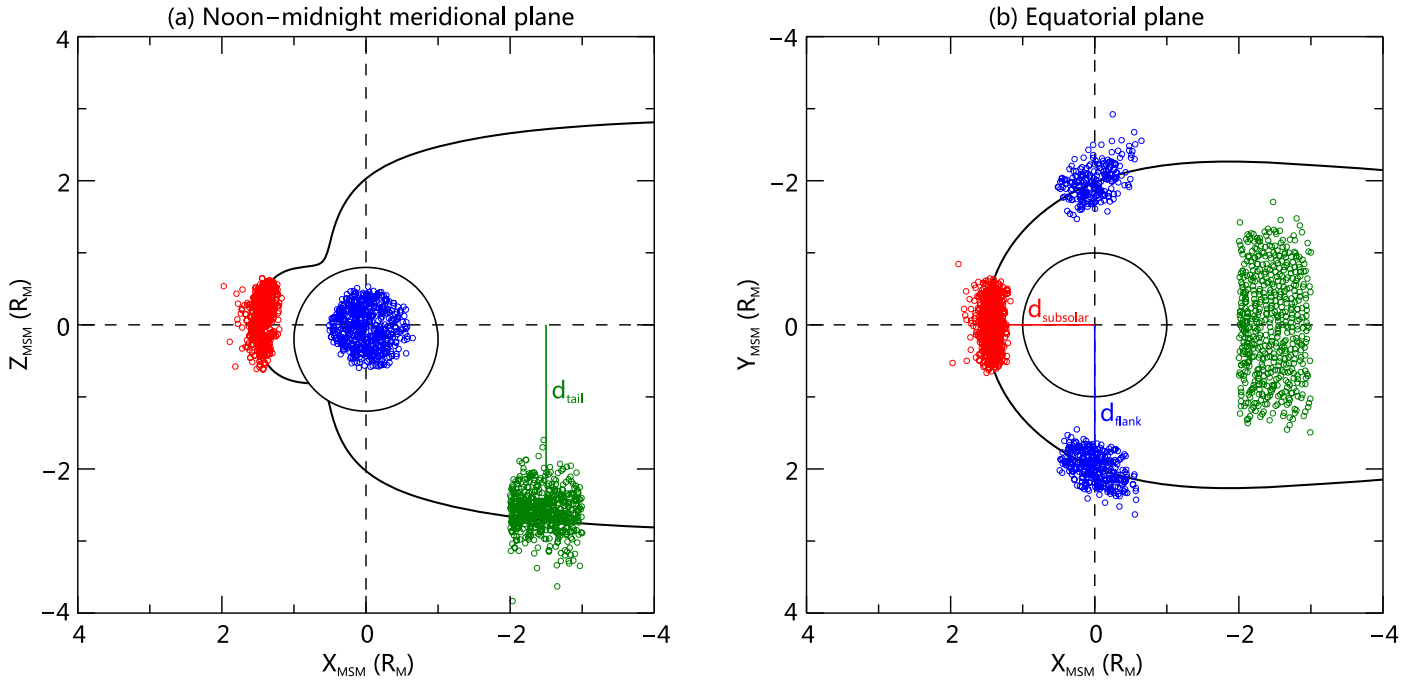

Figure 1. Projection of the observed *MESSENGER* magnetopause crossings onto the aberrated MSM (a) *X*–*Z* and (b) *X*–*Y* planes relative to Mercury's surface (circle) and the average magnetopause from the three-dimensional model (solid lines) (Zhong et al. 2015a). The model predicts that the average magnetopause intersects the planetary surface on the dayside southern hemisphere due to the magnetopause near-cusp indentation and the northward offset of Mercury's dipole. The red, blue, and green circles stand for crossings observed in the subsolar region, the flank region, and the tail high-latitude region, respectively.

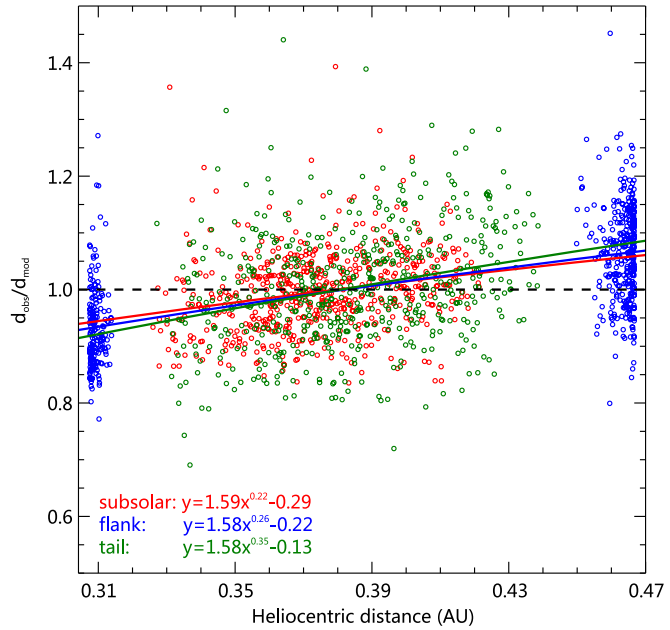

Figure 2. Ratio of the observed dimensions to the average dimensions from the model as a function of heliocentric distance in three regions: subsolar (red), flank (blue), and tail regions (green). The curves are results of the power function ($y = a_0 \cdot x^{a1} + a_2$) fit to the data in the three regions.

clearly decrease with decreasing heliocentric distance, indicating the magnetosphere contracts globally when Mercury moves from aphelion to perihelion.

4. IMF Cone Angle Effect

Due to a lack of an upstream IMF monitor, we use the average value of the magnetic field recorded over 15 minutes outside the outermost bow shock crossings to determine the upstream IMF conditions. The bow shock crossings were identified by visual inspection of abrupt changes in the magnetic field strength and the heated ion flux spectrogram between the solar wind and the magnetosheath (see Figure 9 in Zhong et al. (2015a) and Figure 2 in He et al. 2017). Only cases under quasi-steady IMF conditions, i.e., cases for which the standard deviation of the IMF angles was lower than 10°, were analyzed. To minimize the orbital eccentricity effect, all the magnetopause crossings in each region were mapped to a fixed radial distance, e.g., 0.39 au, from the Sun using the fitted geometric model. The mapped ratios d_{obs}/d_{mod} are plotted as a function of the IMF cone angle in Figure 3. The cone angle is defined as $\cos^{-1}(B_X/|B|)$, approximate to the angle between the IMF and the opposite solar wind velocity vectors. The black dashed parabolic curves ($y = a_3 \cdot (x-90)^2 + a_4$) that emphasize the trends are the fits of all data in the corresponding panels. The standard errors of the best-fit values for the three regions are 0.07 R_M, 0.08 R_M, and 0.09 R_M, respectively. In spite of a large spread of observational data, one can see clearly that the global magnetosphere is influenced by the IMF cone angle. The subsolar distance, flank distance, and tail radius are all outward displacements from the average conditions during the radial IMF (cone angle = 0° or 180°) and inward displacements during the perpendicular IMF (cone angle = 90°). This indicates the magnetosphere expands globally during radial IMF conditions.

To separate the possible IMF B_Z effects from the radial IMF expansion effects, we divided our data set into two subsets according to IMF B_Z sign (Figure 3). The blue points stand for the IMF with the positive B_Z component and the red points are for the negative B_Z component. The average values in each cone angle bin are shown by horizontal bars with corresponding colors. Changes in magnetopause location for the IMF

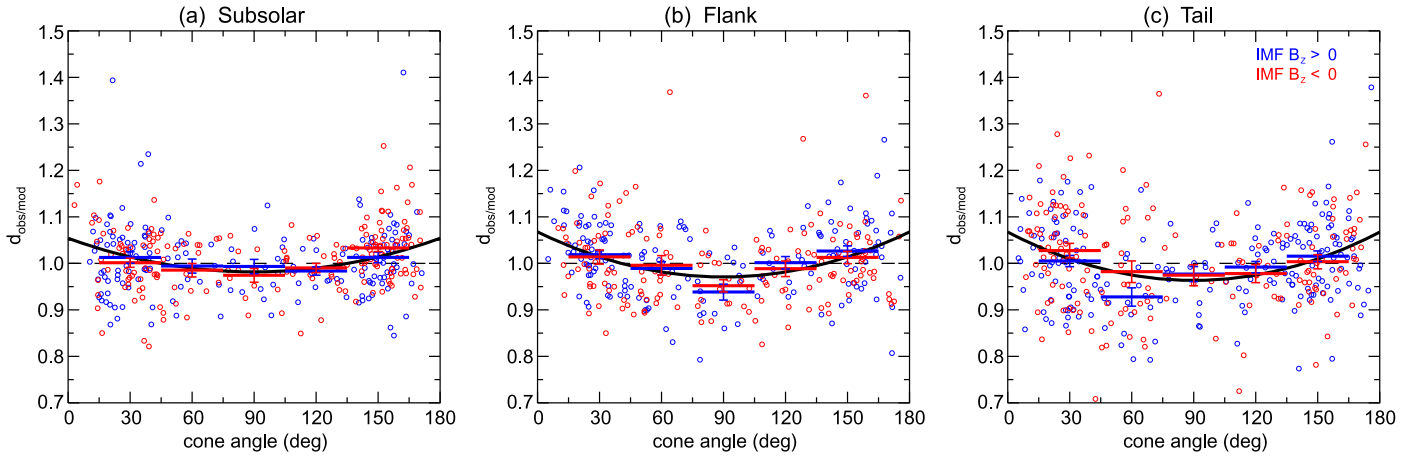

Figure 3. Mapped ratio of the observed dimensions to the average dimensions from the model as a function of the IMF cone angle in the (a) subsolar, (b) flank, and (c) tail southern high-latitude regions. The black dashed curves show the parabolic curve ($y = a_3 \cdot (x - 90)^2 + a_4$) fitting results. The blue (red) points are crossings under positive (negative) IMF B_Z conditions. The horizontal bars show the mean values of each bin, and the error bars represent the standard error of the mean.

Table 1
Best-fit Parameters of the Power Function Model ($y = a_0 \cdot x^{a1} + a_2$) of the Orbital Eccentricity Effect and the Parabolic Curve Model ($y = a_3 \cdot (x - 90)^2 + a_4$) of the IMF Cone Angle Effect

	a_0	a_1	a_2	a_3 ($\times 10^{-5}$)	a_4
Subsolar	1.59 ± 0.05	0.22 ± 0.02	−0.29 ± 0.04	0.89 ± 0.15	0.98 ± 0.01
Flank	1.58 ± 0.05	0.26 ± 0.01	−0.22 ± 0.05	1.20 ± 0.16	0.97 ± 0.01
Tail	1.58 ± 0.05	0.35 ± 0.03	−0.13 ± 0.05	1.28 ± 0.14	0.96 ± 0.01

$B_Z > 0$ and $B_Z < 0$ data sets are not obvious, except for the 45°–75° cone angles in the tail region. It appears that the southern tail magnetopause is displaced inward from its average locations when IMF points sunward and northward (cone angle ≈ 60°, and $B_Z > 0$), leading to an asymmetry between sunward and planetward IMFs. The results suggest that reconfigurations of Mercury's magnetosphere are strongly controlled by the IMF cone angle and to a lesser degree by IMF B_Z.

5. Magnetopause Model

To investigate the effects of orbital eccentricity and IMF cone angle, we construct the average Mercury magnetopause model that ignores the near-cusp indentations:

$$r(\theta, \varphi) = r_0 \left(\frac{2}{1 + \cos\theta} \right)^{\alpha + \beta \cdot \cos^2 \varphi}.$$

The $r(\theta, \varphi)$ is the radial distance from the dipole center to the magnetopause, θ is the polar angle, φ is the azimuth angle, r_0 is subsolar distance, and $\alpha + \beta \cdot \cos^2(\varphi)$ is the level of tail flaring with respect to the azimuth angle, which controls the azimuthal asymmetric magnetopause shape. The azimuth angle is defined as the angle between the projection of r in the Y–Z plane and the direction of the positive Y-axis from $-\pi$ and π clockwise when looking from Mercury to the Sun.

The level of tail flaring thus in the noon–midnight meridional plane is α and that in the equatorial plane is $\alpha+\beta$, which can be calculated from the observed subsolar distance, flank distance, and the tail north–south radius downstream of $X_0 = -2.5\ R_M$:

$$d_{flank} = d_{subsolar} \cdot 2^{\alpha+\beta}$$
$$r_{tail} = d_{subsolar} \cdot \left(\frac{2}{1 + X_0 / r_{tail}} \right)^{\alpha}, \text{ where } r_{tail} = (d_{tail}^2 + X_0^2)^{0.5}.$$

Based on the power function model of the orbital eccentricity effect and the parabolic curve model of the IMF cone angle effect, the dimensions of the three regions as a function of heliocentric distance and IMF cone angle can be described as

$$d = d_0 \cdot (a_0 \cdot r_{SUN}^{a_1} + a_2) \cdot [a_3 \cdot (\theta_C - 90)^2 + a_4],$$

where r_{SUN} is heliocentric distance, θ_C is IMF cone angle, and $d_0 = 1.51\ R_M$, $1.98\ R_M$, and $2.72\ R_M$ are the average dimensions of three regions, respectively. Using a gradient-expansion algorithm to compute a nonlinear least-squares fit to the model (IDL CURVEFIT procedure), the best-fit parameters a_0 to a_4 with standard errors for three regions were obtained (Table 1). The magnetospheric dimensions and the level of tail flaring as a function of heliocentric distance are shown in Figures 4(a) and (b). The shaded region denotes the variations from the effect of IMF cone angle. The tail flaring of the magnetopause in the noon–midnight meridional plane (α) and in the equatorial plane ($\alpha+\beta$) both increase as the magnetosphere expands with increasing distance from the Sun and enhancing IMF radial component. The magnetopause size and shape at perihelion and aphelion, combined with the effect of the IMF cone angle, are compared in Figures 4(c) and (d). Typical magnetopause dimensions for the subsolar, flank, and tail under different conditions are compared in Table 2. Both the orbital eccentricity

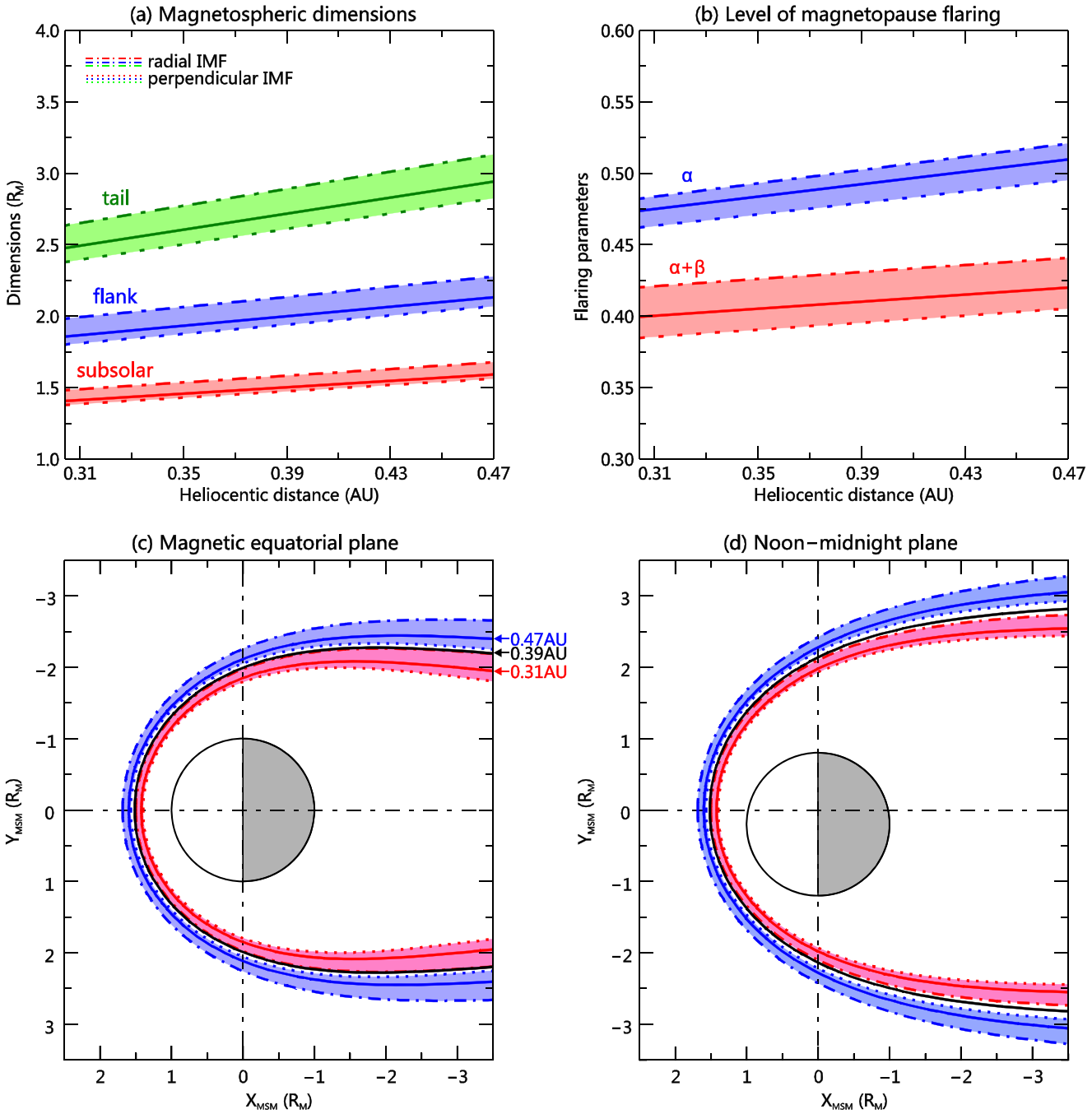

Figure 4. (a) Magnetospheric dimensions as a function of heliocentric distance in three regions: subsolar (red), flank (blue), and tail region (green). (b) The level of tail flaring in the noon–midnight meridional plane (α, blue) and in the equatorial plane ($\alpha+\beta$, red) as a function of heliocentric distance. (c)–(d) Magnetopause shape in (c) the magnetic equatorial plane and (d) the noon–midnight plane at perihelion (0.31 au, red) and aphelion (0.47 au, blue). The average magnetopause shape at 0.39 au (black) is also shown for comparison. The shaded regions show the variations from the effect of IMF cone angle. The upper (or outer, dashed–dotted lines) and lower (or inner, dotted lines) boundaries are under radial and perpendicular IMF conditions, respectively.

effect and the IMF cone angle effect significantly control the size and shape of Mercury's magnetopause.

6. Discussion

With the *MESSENGER* spacecraft's entire orbital data, the statistical analysis shows that the dimensions of Mercury's magnetosphere are significantly influenced by the orbital eccentricity. As Mercury moves from perihelion (aphelion) to aphelion (perihelion) its magnetosphere expands (contracts) globally by ∼15% on average. This orbital variation is, to first order, a response to the average radial changes in solar wind thermal and dynamic pressure and IMF pressure. Like changes in magnetopause shape at Earth (Slavin et al. 1983), the solar wind dynamic pressure compresses the forward magnetosphere and sets the radius of the forward magnetosphere, while the magnetic and thermal pressures compress the nightside magnetosphere and set the radius of the tail.

After normalizing the effects of the orbital eccentricity, we have presented statistical evidence that the IMF cone angle

Table 2
Magnetopause Dimensions for the Subsolar, Flank, and Tail Regions under Different Conditions

	Mean			Radial IMF			Perpendicular IMF		
	0.31 au	0.39 au	0.47 au	0.31 au	0.39 au	0.47 au	0.31 au	0.39 au	0.47 au
Subsolar distance (R_M)	1.43	1.52	1.60	1.50	1.60	1.69	1.40	1.49	1.57
Flank distance (R_M)	1.85	1.99	2.11	1.97	2.13	2.26	1.79	1.93	2.05
Tail radius (R_M)	2.50	2.74	2.95	2.67	2.93	3.15	2.41	2.64	2.84

leads to reconfigurations of the magnetosphere comparable to the changes in solar wind pressure with radial distance from the Sun. The expansion of Mercury's magnetosphere under radial IMF is consistent with Earth models of a globally expanding magnetosphere (Dušík et al. 2010) rather than a bullet-like shape with decreased flaring (Merka et al. 2003). The radial IMF effect can be explained by a reduction of the solar wind dynamic pressure at the magnetopause, which is controlled by IMF orientation (e.g., Samsonov et al. 2012, 2017). The fraction of solar wind pressure applied to the magnetopause at Earth can be extremely small, i.e., ∼20%, during radial IMF conditions (Suvorova et al. 2010), but increase to over 60% during perpendicular IMF conditions (Shue & Chao 2013). The observations presented here suggest that the fraction of solar wind pressure applied to Mercury's magnetopause may also depend on the IMF orientation.

Considering the effects of orbital eccentricity and IMF cone angle, a standard model of Mercury's magnetopause with azimuthal asymmetric shape was developed. In most cases, the level of flaring is lower than 0.5, representing a closed magnetopause, i.e., magnetopause flaring on the dayside that shrinks on the nightside. In addition, the level of flaring decreases with the contraction of the magnetosphere. At 0.31 au, the tail equatorial magnetopause is displaced inward significantly. This indicates that the enhanced solar wind thermal and magnetic pressure can be sufficient to compress the magnetosphere inward where the planetary magnetic field is much weaker. For the Earth's open magnetosphere, self-similar magnetopause shapes are found only for solar wind compression effects (e.g., Shue et al. 1998; Lin et al. 2010). Considering dayside magnetopause reconnection, a decrease in the subsolar distance is commonly accompanied by an increase of magnetopause flaring due to the "erosion" of magnetic flux from the dayside to the nightside magnetosphere (Holzer & Slavin 1978, 1979; Shue et al. 1997).

The reconnection is considered to be more efficient at Mercury than that of Earth, due to the much lower Alfvénic Mach number and plasma beta in the inner solar system (e.g., DiBraccio et al. 2013; Gershman et al. 2013; Slavin et al. 2014; Zhong et al. 2015b; Zhong et al. 2018). Here the comparison of two subsets according to the IMF B_Z sign in Figure 3 may provide some clues about the reconnection effects at Mercury. The "erosion" effects during the southward IMF (cone angle $\approx 90^\circ$ and $B_Z < 0$), i.e., the inward displacement of the subsolar magnetopause and the outward displacements of the flank and tail magnetopause, are not obvious when compared with the northward IMF conditions (cone angle $\approx 90^\circ$ and $B_Z > 0$). One possible explanation is that the solar wind compression effects dominate the "erosion" effects due to the low magnetopause flaring and the weak planetary magnetic field. During the northward/sunward IMF, the reconnection is expected to occur just tailward of the southern magnetic cusp and near the observed tail magnetopause (Slavin et al. 2012). The reconnection-related thermal pressure compression effects (Shue & Chao 2013) may play an important role in the local magnetopause pressure balance, which can explain the observed inward displacement of tail magnetopause under IMF $B_Z > 0$ and cone angle $\approx 60^\circ$. Similar asymmetry cone angle distributions could be expected in the northern high-latitude tail magnetopause, where there is a lack of observations due to *MESSENGER*'s orbit.

7. Summary

We conclude that the large-scale dynamics of Mercury's magnetosphere is dominated by the effects of its orbital eccentricity, but extremely responsive to IMF cone angle. The distinctive reconfigurations of Mercury's magnetosphere are attributed to the relatively small planetary field and the large compressions of the magnetosphere driven by the intense solar wind conditions in the inner solar system. Here we have focused on the long-term average magnetospheric state under quasi-stable IMF conditions. The instantaneous responses of Mercury's magnetosphere, and thus magnetosphere–exosphere-surface coupling to the variability of solar wind, are unlikely to be revealed by a single spacecraft such as *MESSENGER*. The dual spacecraft of the ESA-JAXA BepiColombo mission are particularly well suited to the study of the instantaneous interaction of the solar wind with Mercury's system, as one satellite will be in the upstream solar wind and the other will be in the magnetosphere.

The *MESSENGER* magnetic field data from the Magnetometer (MAG; Anderson et al. 2007) and plasma data from the Fast Imaging Plasma Spectrometer (FIPS; Andrews et al. 2007) are available from the Planetary Data System (https://pds-ppi.igpp.ucla.edu). From there we have used the MAG calibrated data archive (MESS-E/V/H/SW-MAG-3-CDR-CALIBRATED-V1.0, file names MAGMSOSCIXXXXX_V08), and the EPPS derived data archive (MESS-E/V/H/SW-EPPS-3-FIPS-DDR-V2.0, file names FIPS_ESPEC_XXXXXXX_DDR_V0X) to identify the bow shock and magnetopause. A list of bow shock and magnetopause crossings is available upon request to the corresponding author. This work was supported by the Strategic Priority Research Program of the Chinese Academy of Sciences (grant No. XDA17010201) and the National Natural Science Foundation of China (41674178, 41874198, 41621004). J.A.S. was supported by NASA Discovery Data Analysis Grant 80NSSC18K1137.

ORCID iDs

J. Zhong https://orcid.org/0000-0003-4187-3361
H. Zhang https://orcid.org/0000-0002-3680-4989
L. H. Chai https://orcid.org/0000-0001-8844-9176

References

Anderson, B. J., Acuña, M. H., Lohr, D. A., et al. 2007, SSRv, 131, 417
Anderson, B. J., Johnson, C. L., Korth, H., et al. 2011, Sci, 333, 1859
Andrews, G. B., Zurbuchen, T., Mauk, B., et al. 2007, SSRv, 131, 523
Aubry, M. P., Russell, C. T., & Kivelson, M. G. 1970, JGR, 75, 7018
Bedini, P. D., Solomon, S. C., Finnegan, E. J., et al. 2012, AcAau, 81, 369
Burlaga, L. F. 2001, P&SS, 49, 1619
Chang, Q., Xu, X., Xu, Q., et al. 2019, ApJ, 884, 102
DiBraccio, G. A., Slavin, J. A., Boardsen, S. A., et al. 2013, JGRA, 118, 997
Dušík, Š., Granko, G., Šafránková, J., Němeček, Z., & Jelínek, K. 2010, GeoRL, 37, L19103
Fairfield, D. H., Baumjohann, W., Paschmann, G., Lühr, H., & Sibeck, D. G. 1990, JGR, 95, 3773
Gershman, D. J., Slavin, J. A., Raines, J. M., et al. 2013, JGRA, 118, 7181
He, M., Vogt, J., Heyner, D., & Zhong, J. 2017, JGRA, 122, 6150
Holzer, R. E., & Slavin, J. A. 1978, JGR, 83, 3831
Holzer, R. E., & Slavin, J. A. 1979, JGR, 84, 2573
Ip, W.-H., & Kopp, A. 2002, JGRA, 107, 1348
James, M. K., Imber, S. M., Bunce, E. J., et al. 2017, JGRA, 122, 7907
Jia, X., Slavin, J. A., Poh, G., et al. 2019, JGRA, 124, 229
Johnson, C. L., Philpott, L. C., Anderson, B. J., et al. 2016, GeoRL, 43, 2436
Kabin, K., Gombosi, T. I., DeZeeuw, D. L., & Powell, K. G. 2000, Icar, 143, 397
Kallio, E., & Janhunen, P. 2003, GeoRL, 30, 1877
Korth, H., Anderson, B. J., Zurbuchen, T. H., et al. 2011, P&SS, 59, 2075
Lin, R. L., Zhang, X. X., Liu, S. Q., Wang, Y. L., & Gong, J. C. 2010, JGRA, 115, A04207
Massetti, S., Orsini, S., Milillo, A., & Mura, A. 2007, P&SS, 55, 1557
Merka, J., Szabo, A., Šafránková, J., & Němeček, Z. 2003, JGRA, 108, 1269
Milillo, A., Wurz, P., Orsini, S., et al. 2005, SSRv, 117, 397
Orsini, S., Blomberg, L. G., Delcourt, D., et al. 2007, SSRv, 132, 551
Park, J.-S., Shue, J.-H., Kim, K.-H., et al. 2016, JGRA, 121, 6480
Samsonov, A. A., Němeček, Z., Šafránková, J., & Jelínek, K. 2012, JGRA, 117, A05221
Samsonov, A. A., Sibeck, D. G., Šafránková, J., Němeček, Z., & Shue, J. H. 2017, JGRA, 122, 3110
Shue, J. H., & Chao, J. K. 2013, JGRA, 118, 3017
Shue, J. H., Chao, J. K., Fu, H. C., et al. 1997, JGR, 102, 9497
Shue, J. H., Song, P., Russell, C. T., et al. 1998, JGR, 103, 17691
Slavin, J. A., DiBraccio, G. A., Gershman, D. J., et al. 2014, JGRA, 119, 8087
Slavin, J. A., Imber, S. M., Boardsen, S. A., et al. 2012, JGRA, 117, A00M06
Slavin, J. A., Middleton, H. R., Raines, J. M., et al. 2019, JGRA, 124, 6613
Slavin, J. A., Tsurutani, B. T., Smith, E. J., Jones, D. E., & Sibeck, D. G. 1983, GeoRL, 10, 973
Suvorova, A. V., Shue, J. H., Dmitriev, A. V., et al. 2010, JGRA, 115, A10216
Varela, J., Pantellini, F., & Moncuquet, M. 2015, P&SS, 119, 264
Winslow, R. M., Anderson, B. J., Johnson, C. L., et al. 2013, JGRA, 118, 2213
Winslow, R. M., Philpott, L., Paty, C. S., et al. 2017, JGRA, 122, 4960
Zhang, H., Fu, S., Pu, Z., et al. 2019, ApJ, 880, 122
Zhong, J., Wan, W. X., Slavin, J. A., et al. 2015a, JGRA, 120, 7658
Zhong, J., Wan, W. X., Wei, Y., et al. 2015b, GeoRL, 42, 10
Zhong, J., Wei, Y., Pu, Z. Y., et al. 2018, ApJL, 860, L20